Chapter 1
Introduction and Literature Review

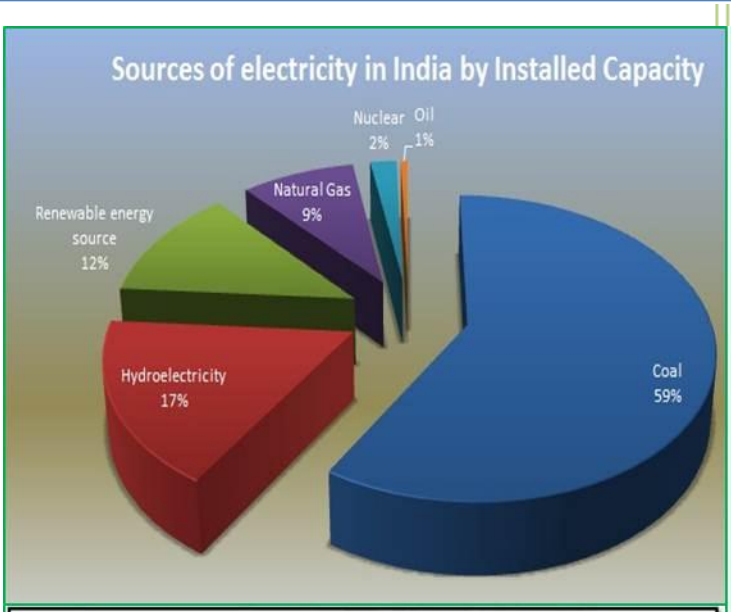

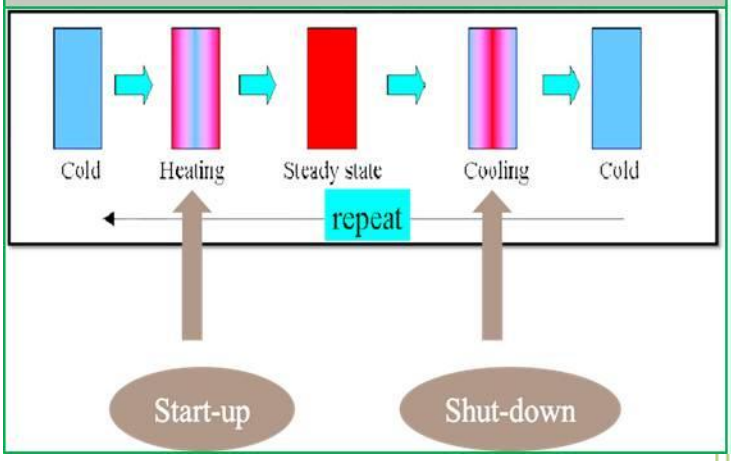

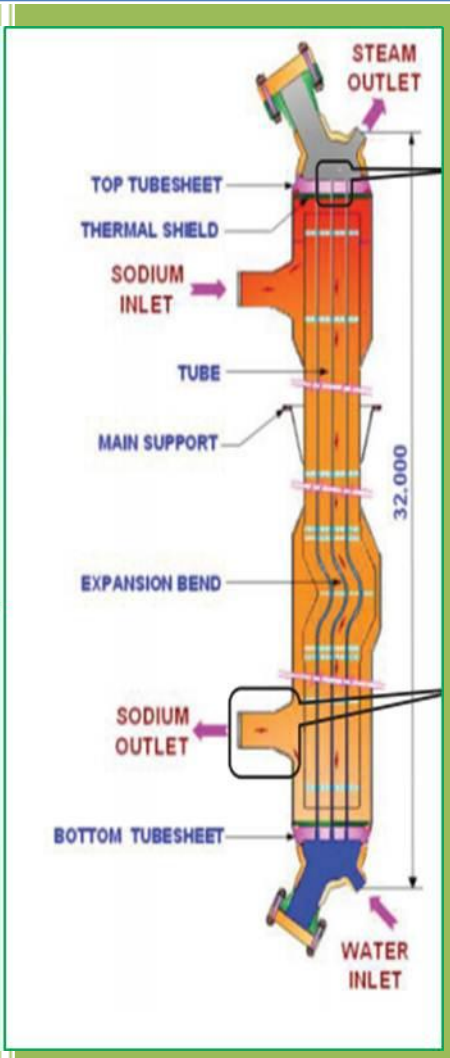

1.1Energy Scenario in India

The dramatic increase in world–wide demand for energy expected in the 21st century has encouraged international cooperation to produce large amount of energy [1]. The generation capacity in India comprises of a mix of coal, hydroelectricity, natural gas, nuclear, and renewable energy sources. Coal is the most important and abundant fossil fuel and it accounts for 59% of the country's energy need. On the other hand, hydro energy and renewable energy resource contributed 17% and 12% respectively [2]. Nuclear energy is the fourth largest source of electricity and it added 2% (Fig. 1.1).

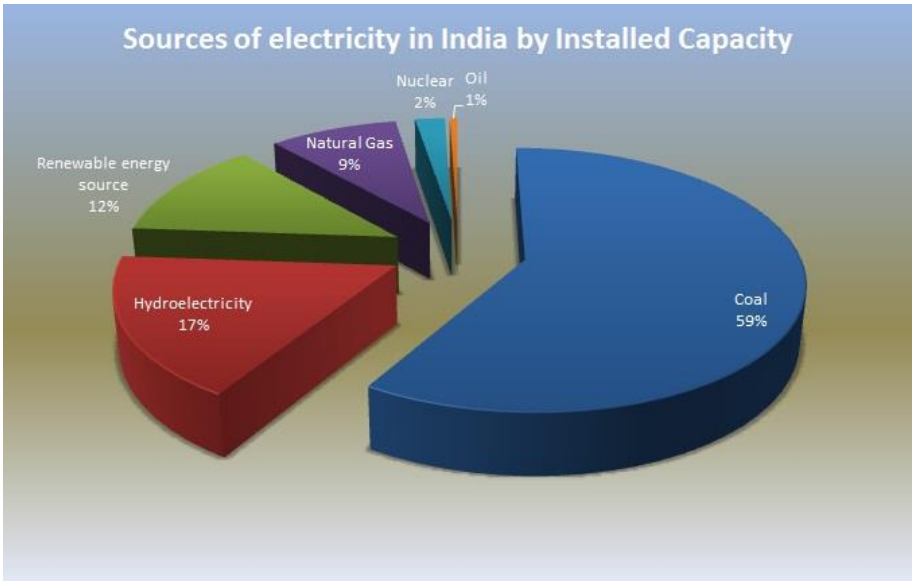

Fig. 1.1 Sources of electricity in India by installed capacity as of 2016 [2].

Comparison of different energy sources for life cycle emissions is shown in Fig. 1.2 [3]. It may be seen that coal has the maximum global warming potential followed by natural gas and others. The developing economy of country promises a sharp increase in energy demands. This will contribute to global warming through large scale greenhouse gas emissions and hundreds of billions of tons of carbon in the form of

carbon dioxide. India's coal production at the present level is sustainable for few decades, so alternative must be developed and brought to the market. Nuclear power is a low carbon energy source and use of nuclear energy can minimize the pollution problem.

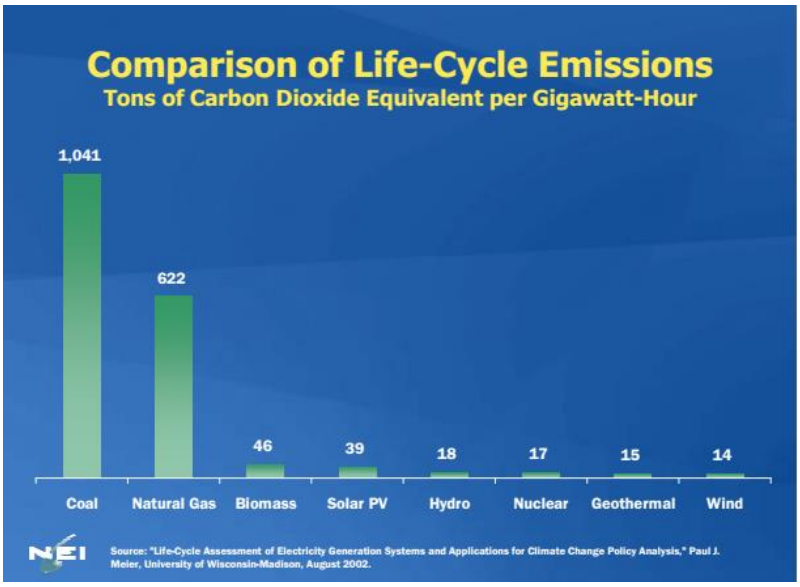

Fig. 1.2 Comparison of life–cycle emissions [3].

At present, nuclear power accounts for only about 2% of electricity generation in India. The Indian government plans to raise nuclear energy's contribution to about 25% of total energy from nuclear power by 2050 [4].

The nuclear energy program in India is being implemented in three stages to utilize its vast thorium source to reduce the carbon foot prints, as shown in Fig. 1.3 [5]. Under the first phase of the programme, a series of pressurized heavy water reactors (PHWRs) with natural uranium oxide as the fuel, have been established. Plutonium generated from PHWRs will be multiplied through breeding in fast breeder reactors

(FBR) in the second stage. This will facilitate launching of a large scale Th–^{233}U fuel cycle in the third stage [6].

Internationally, the fast reactor technology has attained high level of maturity in the last three decades, combinedly with 390 years of successful operation. The emerging international collaborative projects have, therefore, chosen fast reactors as one of the important constituents of the nuclear energy in the 21st century. FBRs are poised to play a major role in the three stage nuclear energy programme of India. Fast breeder reactors constitute the second stage of India's three–stage nuclear energy programme.

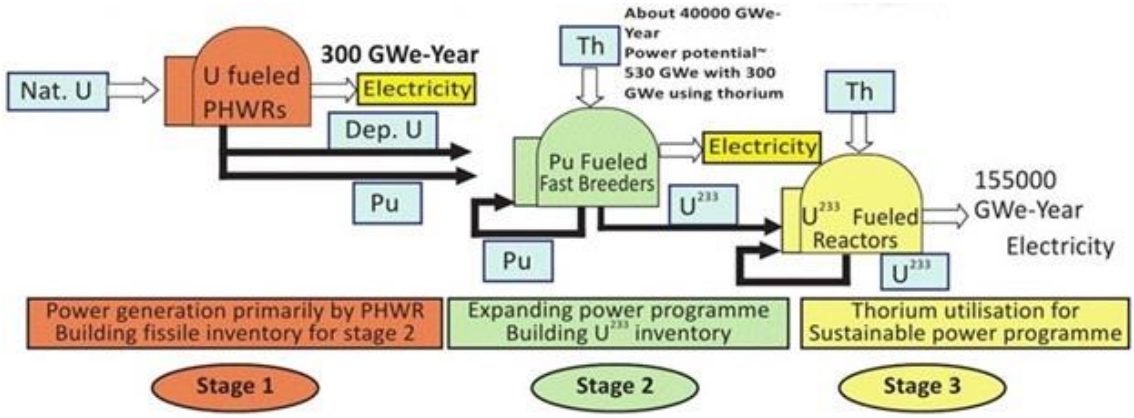

Fig. 1.3 Three stage Indian nuclear power programme.

The PFBR is a 500 MWe, sodium cooled, pool type, mixed oxide (MOX) fuelled reactor having two secondary loops. The reactor is located at Kalpakkam, close to the 2 × 220 MWe PHWR units of the Madras Atomic Power Station (MAPS). Kalpakkam is situated at 68 km south of Chennai on the coast of Bay of Bengal. Schematic of the flow diagram of the PFBR is shown in Fig. 1.4.

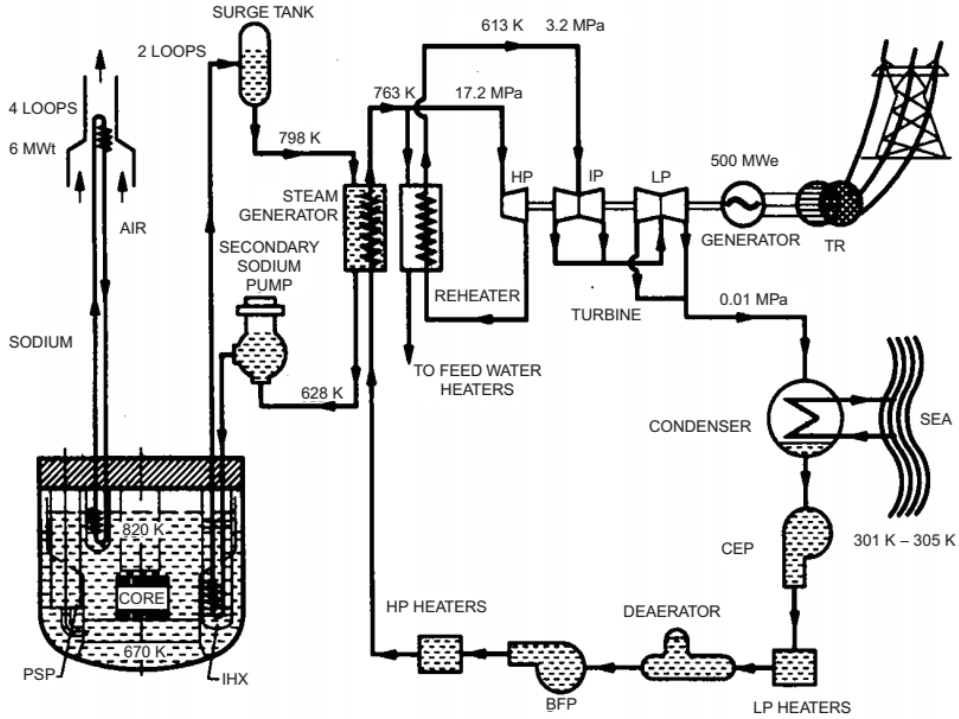

Fig. 1.4 Schematic flow diagram of PFBR showing the major components [6].

1.2 Materials for Fast Breeder Reactor

The core of the reactor consists of fuel subassemblies containing mixed oxide fuel (U, Pu), immersed in a pool of liquid sodium coolant. The heat transport system consists of a primary sodium circuit, secondary sodium circuit and steam–water system. Fast breeder reactor components operate under aggressive and demanding environment of high neutron flux, liquid sodium coolant and elevated temperatures. The integrity of structural materials of these components is vital in the successful and safe operation of FBRs. Table 1.1 shows principal selection criteria for FBR materials.

Table 1.1 Principal selection criteria for FBR structural materials [7].

Mechanical properties	Tensile strength
	Creep
	Low cycle fatigue
	Creep–fatigue interaction
	High cycle fatigue
Design	Inclusion in RCC–MR/ASME design codes
Other properties	Structural integrity
	Weldability
	Workability
	Availability
	Cost

1.2.1 Fuel Assembly

The fuel assembly consists of fuel cladding and wrapper tubes (Fig. 1.5). These core components are subjected to intense neutron irradiation with neutron flux levels of 10^{15} n/cm^{2}s^{-1} which is about two orders of magnitude higher as compared to those of thermal reactors. The core components like grid plate may see a fast fluence of 10^{21} to 10^{22} n/cm^2/s^{-1}. This leads to unique problems in the materials such as void swelling, irradiation creep and helium embrittlement. The operating temperature range for the fuel clad tubes is around 400–700 °C under steady state conditions and in transient condition it may rise to 1000 °C. Fuel clad experiences major loads of 5 MPa by the internal pressure developed due to the accumulation of fission gases released from the fuel

matrix. In transient over power incidents some additional stresses developed due to moderate fuel clad interaction [8].

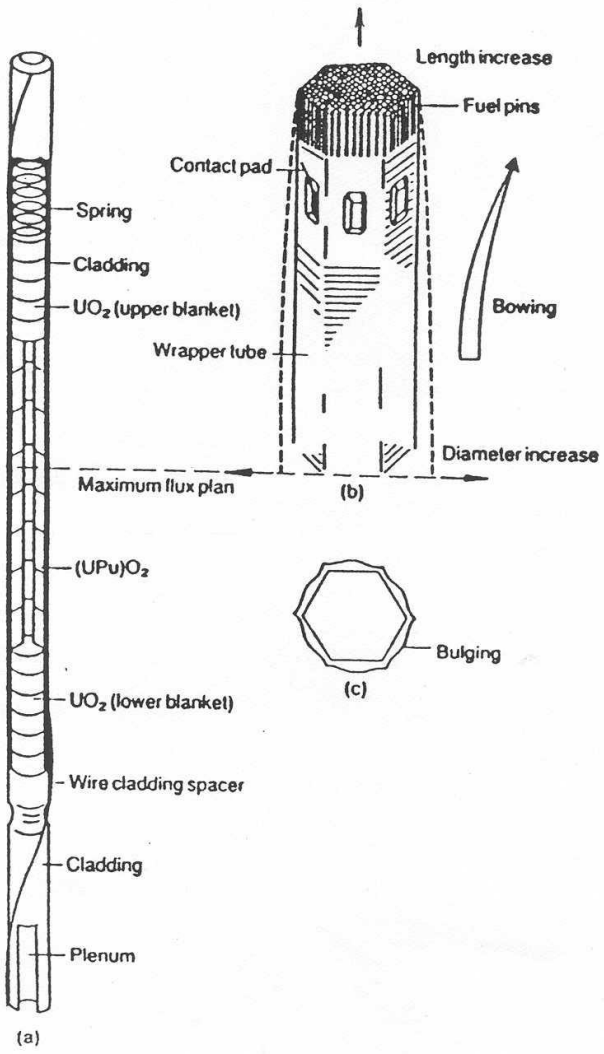

Fig. 1.5 FBR Fuel assembly [8].

The wrapper tubes of the core subassembly, in the steady state operation, experience relatively lower temperatures (400–600 °C) and stress levels of about 0.6 MPa. In transient conditions the temperature may rise to maximum 800 °C. The principal loads on the wrapper tubes arise by the internal pressure from the sodium coolant and the interaction loads at the contact pads due to bowing of the subassemblies

under temperature and swelling gradients. The both clad tubes and wrapper tubes experience peak neutron dose of about 85 dpa. Therefore, the materials required for core components should possess high temperature strength, resistance to void swelling, irradiation creep, and irradiation embrittlement [6].

On the other hand materials for structural components such as reactor vessel, grid plate, pumps and heat exchanger, where irradiation effect is not a vital parameter, must possess good high temperature low cycle fatigue resistance and creep strength in liquid sodium coolant environment. The molten sodium coming from the core components are at different temperatures, falls on the component surface and produces significant variation in the surface temperature and stress, which can cause thermal stripping and lead to high cycle fatigue. This is another important parameter to be considered for materials chosen for structural components above the core.

1.2.2 Core Materials

Earlier days austenitic stainless steels were mainly chosen as the major structural materials for prototype and commercial FBRs owing to their adequate high temperature mechanical properties, compatibility with liquid sodium coolant, good weldability, availability of design data and above all the fairly vast and satisfactory experience in the use of these steels for high temperature service. Different steels developed for the reactor applications are shown in Table 1.2. In general 316 austenitic stainless steels with 20% cold work has been considered a standard material for cladding and wrapper in FBRs. However, its void swelling resistance is poor as required for large burn up for economic operation of FBR. To improve void swelling resistance, 316 stainless steel has been modified with addition of titanium, known as Alloy D9 (ASTM designation A771/UNS S38660). The alloy D9 was further optimized by addition of specific

alloying elements P, Si and B to improve its resistance against void swelling resistance and is known as version D9I.

It has been confirmed from the different irradiation experimental programmes (Phenix–France, PFR–UK, BN600–Russia) that high chromium ferritic–martensitic steels were found to be superior for swelling and irradiation creep resistance up to a dose of around 200 dpa [9,10].

Table 1.2 Different grades of austentic steels used in prototype fast breeder reactor [6].

Grade	**Product**	**Applications**
316L (N)	Plate	Main Vessel, Inner vessel, IHX, etc.
304L (N)	Plate	Tanks
304L (N) **316L (N)**	Forging	Heat exchanger, tube, Sheet, pumps
316L (N)	Seamless tubes	Heat exchangers
304L (N) **316L (N**	Seamless pipes	Sodium and gas piping
316L (N)	Round/ Hollow bars	Control rod drives, Fuelling machines
Modified ASS **(Alloy D9)**		Cladding and wrapper materials

The different ferritic–martensitic steels along with their chemical composition investigated under these programmes are presented in Table 1.3a &1.3b. These have excellent void swelling and irradiation creep resistance but their creep resistance decreases drastically above 550 °C. Therefore, they are not suitable for clad tubes but

can be used as a wrapper material because it operates in the lower temperature range. However, the increase in ductile to brittle transition temperature (DBTT) due to irradiation is a cause of concern for ferritic steels.

Table 1.3a Different grades of ferritic steels for in–core components fast breeder reactors [11].

Reactor	**Country**	**Cladding Material**[a]	**Wrapper Material**[a]
PFR	UK	STA Nimonic PE16	FV448
PHENIX	France	CW 15Cr–15Ni Ti MoB	EM10
PHENIX	Germany (DEBENE)	CW and CWA 1.4970 Mod.[b]	1.4914[b]
FFTF	USA	HT9	HT9
BN350 BN600	Russia	CW ChS–6.8	EP450
Long Life Cores (proposed)	Japan	PNC–FMS	PNC–FMS

[a]Solution treated and aged Nimonic PE16; 17Cr–43Ni–3Mo 2.5(Ti+Al)–balance Fe

Cold worked (CW) and cold worked and aged (CWA) 1.4970 austenitic stainless steel and modified versions; 15Cr, 15Ni, 1.2Mo, 0.4Ti, 0.005B

Cold worked (CW) ChS–6.8 austenitic Steel: 15–16.5Cr, 14–15.5Ni, 1.9–2.5Mo, 0.2–0.3Ti, 0.001–0.005B

[b] Experimental subassembly

Table 1.3b The chemical compositions of ferritic/martensitic steels (wt%) [11].

HT9	12Cr–0.6Ni–1Mo–0.3V–0.5W
PNC–FMS	11Cr–0.4Ni–0.5Mo–0.2V–0.05Nb–0.05N
FV448	10.7Cr–0.65Ni–0.6Mo–0.15V–0.25Nb
EM10	9Cr–0.2Ni–1Mo
1.4914	10.5Cr–0.85Ni–0.55Mo–0.25V–0.2Nb–≤ 0.01N–≤ 0.0015B
EP450	11–13.5Cr, 0.5–0.3Ni, 1.2–1.8Mo, 0.3–0.6Nb, 0.1–0.3V, 0.004B

1.3. Development of Cr–Mo Steels: Materials for Steam Generator

1.3.1 Steam Generator of FBR

The steam generator (SG) is a vertical, countercurrent shell–and–tube type heat exchanger with sodium on shell side, flowing from top to bottom, and water/steam on tube side. The schematic of SG is shown in Fig. 1.6a. Usually a mono–metallic component (tube, shell and thick section tube–sheet/plate) is fabricated to avoid tube to tube sheet welds, which are critical regions of the component failure and has been used in Indian PFBR. In SG, molten sodium enters with temperature of ≈525 °C through a single inlet nozzle and initially flows upward in the annular region and then flows downwards through the top plenum where it is evenly distributed before entering the shell side of the SG. After flowing across the tube bundle, the cold sodium exits at 355 °C through the bottom outlet plenum and a single outlet nozzle. Water enters the tube side from the bottom tube sheet at 235 °C and flows upward. Superheated steam exits the SG through the top tube–sheet and the nozzle at top dished end at 493 °C (Fig. 1.6b) [12]. These operating temperatures give a differential temperature of 120 °C across bottom tube sheet of the SG. Table 1.4 shows the operating condition parameters of SG in FBR.

High–pressure water in the tube is heated from outside by high temperature of sodium in the SG of FBR. In the case of loss of feed water flow to the SG due to the tube failure, the high–pressure water/steam leaks into sodium and sodium–water reaction occurs. In case of this incident the hot sodium at 525 °C from the oil fired sodium heater will flow through the SG and result in thermal shock to the thick components like bottom tube sheet. Some past FBR plants experienced the sodium–water reaction due to failure of the SG tube [13,14]. Because of the consequences of high reactivity of sodium with water SG was considered as an important component in determining the efficient and safe running of the FBR plant and demands high integrity of SG components.

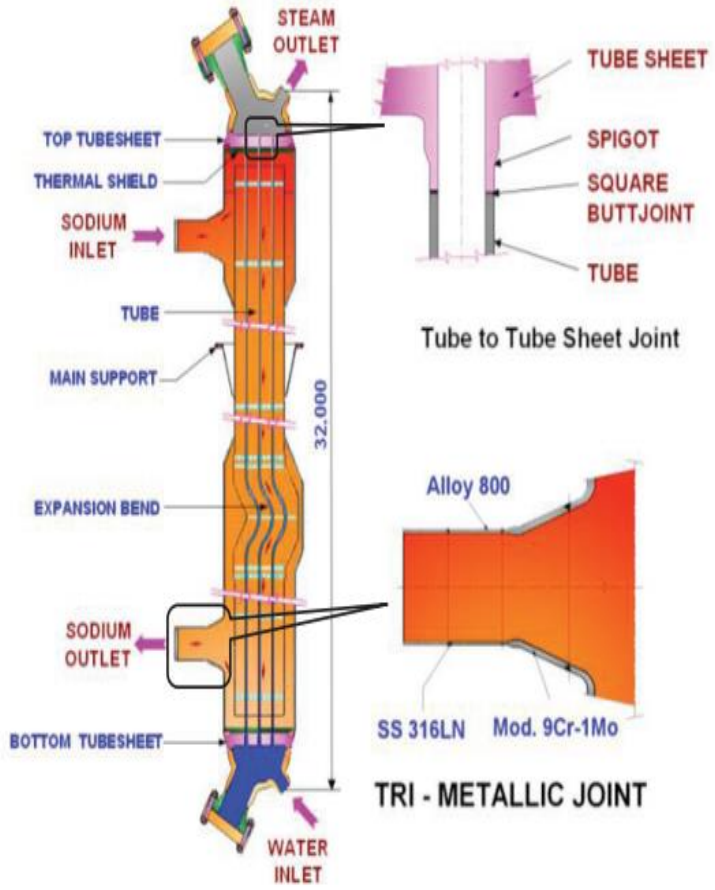

Fig. 1.6a Schematic arrangement of steam generator [12].

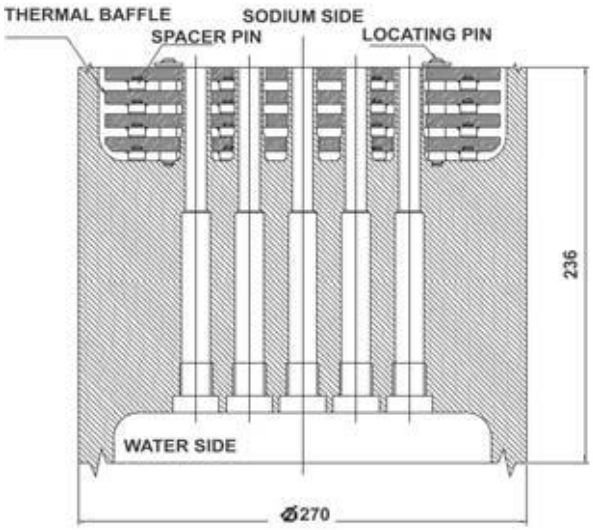

Fig. 1.6b Schematic arrangement of steam generator bottom tube sheet [15].

Table 1.4 Description of steam generator in PFBR [16].

Thermal power per SG(MW)	157.9
No. of steam generators/plant	6
Design life (Years)/ cap. Factor	40/75%
Tube length (m) / No. of tubes	23/547
Tube size (inner diameter/thickness)	12.3/2.3
Pitch	32.2
Shell inner diameter (mm)	831
Effective heat transfer area (m^2)	652
Water side mass flux (kg/m^2s)	1030
Steam outlet velocity (m/s)	17.8
Tube side pressure drop (bars)	2.80
Shell side pressure drop (bars)	0.6
Critical heat flux (Inner diameter) (kW/m^2)	579
Peak heat flux (Inner diameter) (kW/m^2)	694
Total number of tubes to tube sheet joints required	8752
Specific heat consumption (T/MWe)	-0.756

1.3.2 Development of Cr–Mo Steels

Since the last seven to eight decades Cr–Mo steels have been widely used in the electrical power–generating industries, nuclear power plants and chemical and petroleum processing industries [17,18]. When the need for creep–resisting steels arose in the late 1930s, the Cr–Mo steels were a natural progression from the carbon steels when C–Mn steels were in common use. Addition of 0.50% Molybdenum to carbon steel was seen to enhance the creep strength, however, had inadequate ductility and tendency for graphitization. Molybdenum concentrations were eventually increased to 1% to improve creep strength which also enhanced the ductility and eliminated graphitization. To maintain ductility and increase oxidation resistance at higher operating temperatures, more chromium was also added.

It was believed that molybdenum concentration of 1% and Cr of minimum 2% was believed to be optimum for high temperature strength and oxidation respectively for applications up to 550–600°C [19]. Alloys with higher chromium concentrations such as 5Cr–½Mo, 7Cr–½Mo, 9Cr–1Mo, and 12Cr–1Mo were developed for operation in more aggressive atmospheres (e.g., in the petrochemical and oil industry).

The addition of more chromium (above 2¼%) to the Cr–Mo steels increases the hardenability of the steel and for a Cr content of 9% the steel can be air hardened to entirely martenisitic structure in the normally used section sizes [19]. Furthermore, the oxidation and corrosion resistances increase gradually with chromium content. However, no large improvement in corrosion resistance occurs until the 12% Cr. However, in that condition it must be tempered before it can be fabricated. The other alternative is to use an annealed product. In either case, the creep properties rather quickly approach those of 2¼Cr–1Mo steel [19,20]. According to Orr et al. [19] the carbide present in 9Cr–1Mo steel after normalizing and tempering is predominantly

$M_{23}C_6$; a small amount of M_7C_3 also forms. Although there are some indications that MC may be present early in a tempering treatment, it is quickly replaced by the more stable chromium–rich carbides. The $M_{23}C_6$ rather quickly agglomerates (Ostwald ripening), which gives rise to a loss of strength [19]. Similarly, $M_{23}C_6$ is the predominant precipitate in 12%Cr–1Mo steel. It is these facts that account for the widespread use of 2¼Cr–1Mo steel relative to the higher–chromium steels for elevated temperature strength to ≈550 °C.

1.3.3 Material Properties Required for SG

Selection of proper material, optimized design and fabrication are crucial to have high integrity of SG components. Properties required for steam generator material are given below:

- Low thermal expansion co–efficient
- High thermal conductivity
- High tensile strength,
- High creep strength
- High low cycle fatigue resistance
- Less damage from creep–fatigue interaction
- High structural integrity
- Good weldability
- High workability
- Easy availability
- Lower cost

In addition the material should possess resistance to loss of carbon to liquid sodium which can lead to reduction in strength; resistance to wastage in case of small leaks

leading to sodium–water reaction and resistance to stress corrosion cracking in sodium and water media [21].

1.3.4 Cr–Mo Steels for SG

Cr–Mo steel in nuclear fast reactor applications was introduced since last 4 decades after the development of 9–12%Cr–Mo steel, because of its superior thermal conductivity and low coefficient of thermal expansion compared to austenitic steels. These steels also have excellent strength and toughness at low temperatures and have elevated temperature creep resistance in combination with good corrosion resistance [22,23]. Their elevated temperature properties make them economically attractive in comparison to that of austenitic stainless steels and high–nickel alloys up to about 600 °C [24]. Cr–Mo–C steels can be modified by the addition of carbide–forming elements to further enhance the high temperature mechanical properties and microstructural stability [25]. Furthermore, ferritic steels, including several Cr–Mo steels, have been found to have excellent neutron void swelling resistance to heavy ions or irradiation in a fast reactor environment conditions. These attractive properties of Cr–Mo alloys are of interest for fast breeder reactors[17,18].

Comparison of neutron void swelling resistance of ferritic and austenitic steels with fluence is shown Fig. 1.7 [26] It may be seen significantly higher resistance to swelling in ferritic steels than austenitic steels. Besides their excellent neutron irradiation void swelling resistance the Cr–Mo steels have excellent resistance to thermal stresses which makes them a candidate material for first wall and blanket structural material for fusion reactors design [27], where large thermal gradients could lead to cyclic fatigue and creep–fatigue damage within a strong neutron radiation field. For Indian PFBR steam generator, a range of materials starting from ferritic steels (2.25Cr–1Mo, Nb stabilised 2.25Cr–1Mo, 9Cr–1Mo (grade 9), Modified 9Cr–1Mo

(grade 91)) austenitic stainless steels (AISI 304/316/321) and alloy 800 were investigated [28].

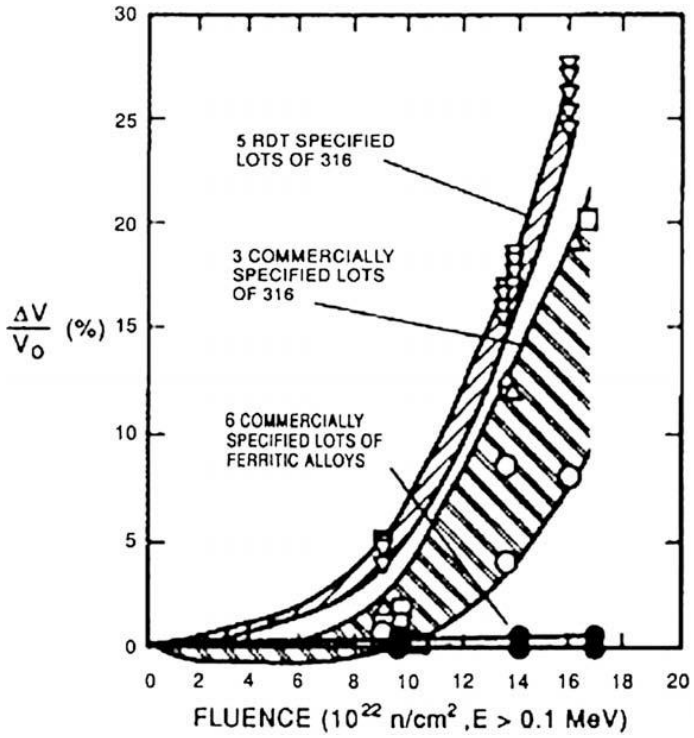

Fig. 1.7. Volumetric swelling vs. neutron fluence in austenitic and ferritic steels [26].

In view of the poor resistance to aqueous stress corrosion cracking (SCC), austenitic stainless steels of 300 series were not considered for the steam generator. Alloy 800 shows better resistance to SCC than austenitic steels, but it is not immune to stress corrosion cracking in chloride and caustic environments. Therefore, ferritic steels are the most preferred materials for steam generator applications (Table 1.5). Among the ferritic steels 2.25Cr–1Mo and 9Cr–1Mo steels, modified 9Cr–1Mo (grade 91) was preferred for SG components. The selection of modified ferritic steels is essentially based on superior high temperature strength and better creep resistance, due to the presence of Nb and V, in comparison to the conventional 9Cr–1Mo steel. Figure 1.8

shows the creep rupture strength of several austenitic and ferritic steels for 10^5 h. Higher creep rupture strength may be seen for ferritic steels as compared to austentic steels, with further superior creep strength of modified 9Cr–1Mo steels. Furthermore, 9Cr–1Mo steels have excellent microstructure stability over a large section size [29–31].

In the design of SG tubes another important aspect is to have improved heat transfer and low thermal stresses across the cross section. Thermal stresses can be reduced with less thick components.

Table 1.5 Materials selected for steam generator in major FBRs [7].

Reactor	**Sodium Inlet Temperature (K)**	**Steam Outlet Temperature (K)**	**Tubing Material**	
			Evaporator	**Superheater**
Phenix	823	785	2.25Cr–1Mo 2.25Cr–1Mo stabilized	321 SS
PFR	813	786	2.25Cr–1Mo stabilized Replacement unit in 2.25Cr–1Mo	316 SS Replacement unit in 9Cr–1Mo
FBTR	783	753	2.25Cr–1Mo stabilized	
BN–600	793	778	2.25Cr–1Mo	304 SS
Super Phenix–I	798	763	Alloy 800 Once through integrated	
MONJU	778	760	2.25Cr–1Mo	304SS
SNR–300	793	773	2.25Cr–1Mo stabilized	2.25Cr–1Mo stabilized
CRBR	767	755	2.25Cr–1Mo	2.25Cr–1Mo
DFBR	793	768	Modified 9Cr–1Mo (grade 91) Once through integrated	
EFR	798	763	Modified 9Cr–1Mo (grade 91) Once through integrated	
PFBR	798	766	Modified 9Cr–1Mo (grade 91) Once through integrated	

The modified steels have twofold allowable stresses than that of 2.25Cr–1Mo and conventional 9Cr–1Mo steels at temperatures of 550 °C and above. This enables substantial reduction in wall thickness of SG tubes, with consequent advantages in terms of enhanced heat transfer and reduced thermal stresses.

The steam generator components such as SG tube, top and bottom tube sheets and shell, thermal baffles are made with modified 9Cr–1Mo steel. The superheater portions are constructed either from 2.25Cr–1Mo, 2.25Cr–1Mo–Nb. As the temperatures are lower in evaporator portion, there is no incentive to use high chromium steels (9Cr–1Mo, 9Cr–1Mo–Nb–V). These considerations favored the initial choice of 2.25Cr–1Mo and 9Cr–1Mo steels as reference materials for evaporator and superheater portions respectively for the PFBR steam generator.

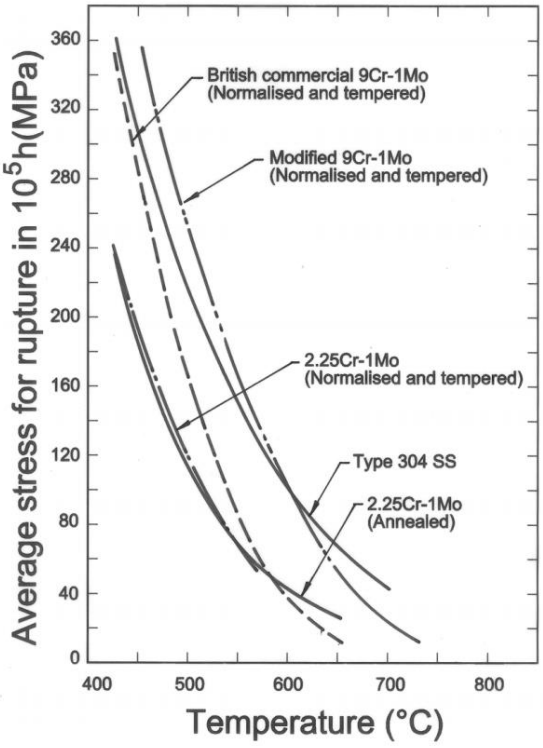

Fig. 1.8 Comparison of creep rupture strength of several materials for 10^5 h [28].

1.4 Physical Metallurgy of Cr–Mo Steels

The structural properties of any material are sensitive to the microstructure and can be altered by addition of alloying elements and specific simple heat treatment procedures. The addition of alloying elements had significant influence on the iron–carbon system. Addition of chromium does not only improve the corrosion resistance but also the resulting microstructure and the mechanical properties. Figure 1.9 shows the schematic pseudo–equilibrium phase diagram for the Fe–Cr–0.1%C system [32,33]. It reveals that the steel with 9% Cr exists in one of the several sub–liquidous phase fields depending on the temperature [32,33]. At high temperature (> ~1473K) δ–ferrite + austenite; and from ~1473K to ~1073K austenite phase; at low temperatures ~1073K–1000K, there is α–ferrite (pro–eutectoid) + γ + primary carbides; and low temperatures (< ~1000K) α–ferrite + primary carbides phases exist. The extent of any phase field present in a particular alloy is dependent on its composition, which can be viewed in terms of a net chromium equivalent derived from the combined effect of ferrite and austenite stabilizing elements [34].

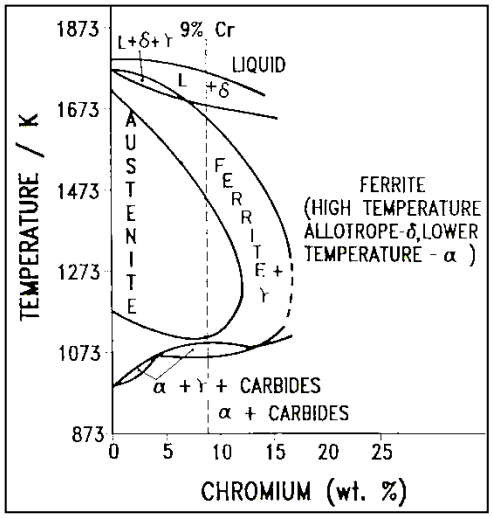

Fig. 1.9 Schematic pseudo–equilibrium Fe (with 0.1%C) –Cr phase diagram [33]. The dashed line indicates the phase fields for steel for 9% Cr.

In ferritic steels various microstructures (martensite, bainite, proeutectoid ferrite, or pearlite) can be developed by heat treatment and significantly affect their mechanical properties. The effect of a given heat treatment is most easily explained by reference to an isothermal–transformation phase diagram or a continuous cooling transformation (CCT) phase diagram. A continuous cooling transformation phase diagram for 9Cr–1Mo steel (Fig. 1.10) shows a wide range of cooling rates to form martensite [35,36].

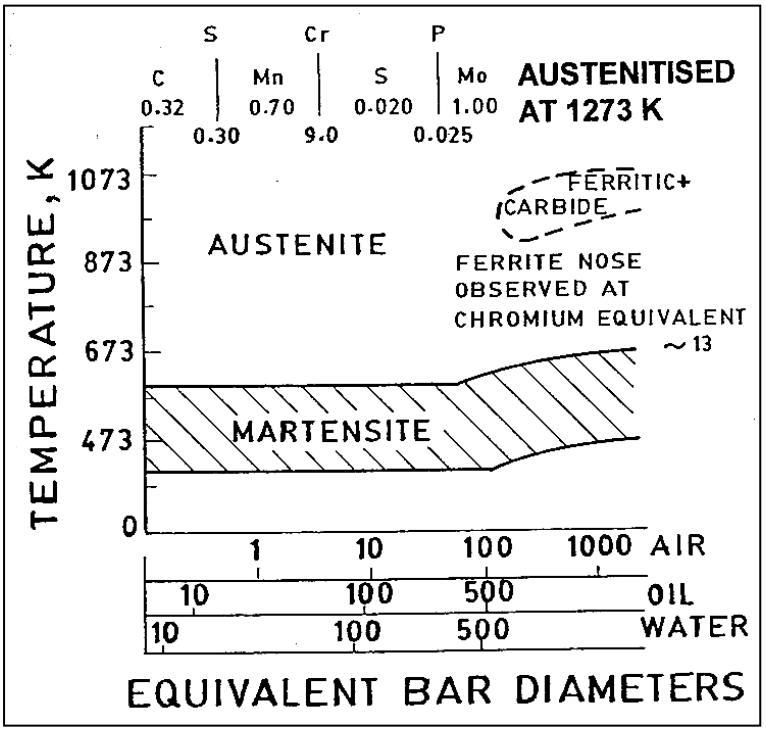

Fig. 1.10 Continuous cooling transformation diagram for 9Cr–1Mo steel [36].

1.4.1 Effect of Alloying Elements and Microstructure

The microstructure of 9Cr–1Mo steel has been studied by several investigators [37,38]. This steel in austenitised and tempered conditions generally exists in lath

martensitic structure with very high dislocation density. Precipitates of carbides type $M_{23}C_6$ are generally found to be distributed inside the martensitic laths and also along the inter–lath boundaries. A modified 9Cr–1Mo steel (Grade 91in both ASTM and ASME) with strengthening elements such as Mo, V and Nb added to conventional 9Cr–1Mo steels is finding increasing applications in power generation industries [24]. Addition of too much of these elements to modified 9Cr–1Mo steels, leads to formation of delta ferrite, which lowers the strengthening effects [39].

Addition of chromium improves the corrosion resistance and mechanical properties. Mo is a solid solution strengthener and is considered a retardant for dislocation recovery/recrystallization [40].

The addition of Nb improves the properties by promoting nucleation of finely distributed $M_{23}C_6$ carbides and refinement of grain size. Addition of V enters the carbide particles and retards their growth. It must be mentioned that in this alloy, strength in normalized and tempered condition is derived from carbides like NbC, VC and $M_{23}C_6$ on sub–boundaries and from the tempered martensitic laths with high dislocation densities. In addition, V and Nb could also form fine precipitates of nitrides/carbonitrides within the ferrite matrix contributing to further strengthening [22].

There are conflicting results on the addition of Ni in Grade 91. The addition of Ni is effective to reduce the amount of delta ferrite. Tsuchida et al. [41] reported that addition of Ni to Grade 91 causes decrease in creep strength of the steel by formation of retained austenite in the normalized state due to the carbon and nitrogen transfer from martensite to austenite. In contrary, Santella et al. [42] reported that retained austenite increased creep strength of weld deposit due to formation of un–tempered martensite even after the adequate heat treatment. They showed on a basis of thermo–expansion

measurements that M_s and M_f points of a standard Grade 91 were about 400 and 200 °C, respectively, and martensitic transformation of Grade 91 almost finished at 200 °C [43]

1.5 Low Cycle Fatigue in Service of SG

In general, structural components operated at high temperature experience thermal stresses because of the difference in temperature from the outer surface to inner core of the component. These thermal stresses are higher than the yield stress of the material and causes low cycle fatigue (LCF) damage in the material. LCF damage occurs due to the start–up and shutdown operation cycles of the component. Pictorially LCF damage in service condition of SG component in a reactor can be explained from Fig. 1.11.

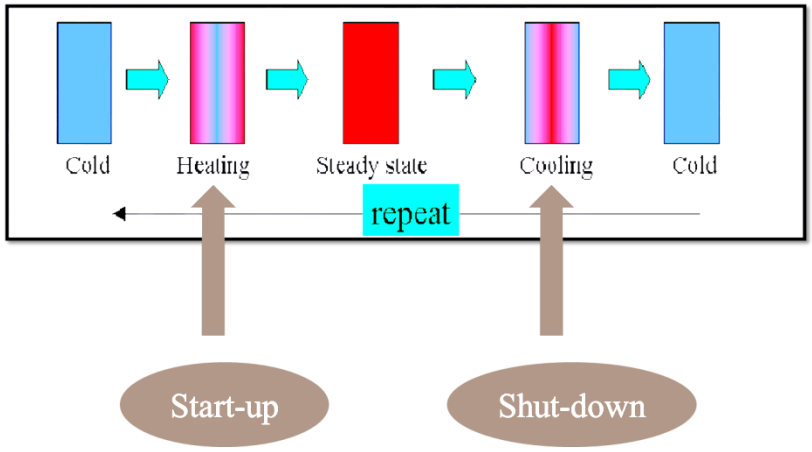

Fig. 1.11 LCF during start–up and shutdown of steam generator structural components.

This start–up and shutdown cycles cause LCF damage in the material. So LCF study of this material is important. In case of transient conditions the increase in thermal stresses and temperature becomes much higher than that of the normal operating condition.

At high temperatures fatigue damage and life are influenced by several time–dependent mechanisms such as dynamic strain ageing (DSA), oxidation, creep and stress induced precipitation occurring concurrently with cyclic loading. These damage processes are strong functions of temperature and strain rate. The occurrence of DSA, which involves interaction of solutes with mobile dislocations during high temperature low cycle fatigue in certain range of temperature and strain rate, leads to reduction in strain controlled fatigue life [44].

Structural materials for out–of–core nuclear system supply system (NSSS) components of sodium cooled fast reactors (SFRs) are chosen mainly on the basis of their high temperature LCF and long term creep properties as well as compatibility with the liquid sodium coolant. Austenitic stainless steels are used for all the NSSS components, except the steam generator for which modified 9Cr–1Mo steel is chosen because of its resistance to stress corrosion cracking [45].

1.6 Dynamic Strain Ageing

Dynamic strain ageing (DSA) is a process of ageing that takes place during plastic deformation over a particular strain rate and temperature range, where the interactions between solute atoms and dislocations, result in a strong pinning of dislocations. A material exhibiting DSA requires higher stresses to produce further straining of the material, either to pull dislocations free from the pinning atoms or to nucleate fresh dislocations. Observation of serrated plastic flow during straining is most common characteristic feature of DSA. There is other phenomena which can give rise to serration in tensile loading such as twinning. [46]. Depending on the material and experimental conditions there could be different types of serrations and their characteristics features are well known. The type of serrations provides useful information to evaluate the kind of atoms that interact with dislocations to cause DSA.

There are five types of serrations (A, B, C, D and E) reported due to DSA and these are shown in Fig. 1.12a.

Type A Serrations: These are periodic serrations characterized by an abrupt increase followed by a drop to below the general level of the stress-strain curve, observed due to repeated deformation bands initiating and propagating from one end of the specimen in the same direction along the gauge length. These are considered as locking serrations. They occur in the low temperature (high strain rate) part of the DSA regime.

Type B Serrations: These are oscillations about the general level of the stress–strain curve that occur in quick succession due to discontinuous band propagation arising from moving dislocations within the band. Usually these occur at the onset of serrated yielding at high temperatures and low strain rates.

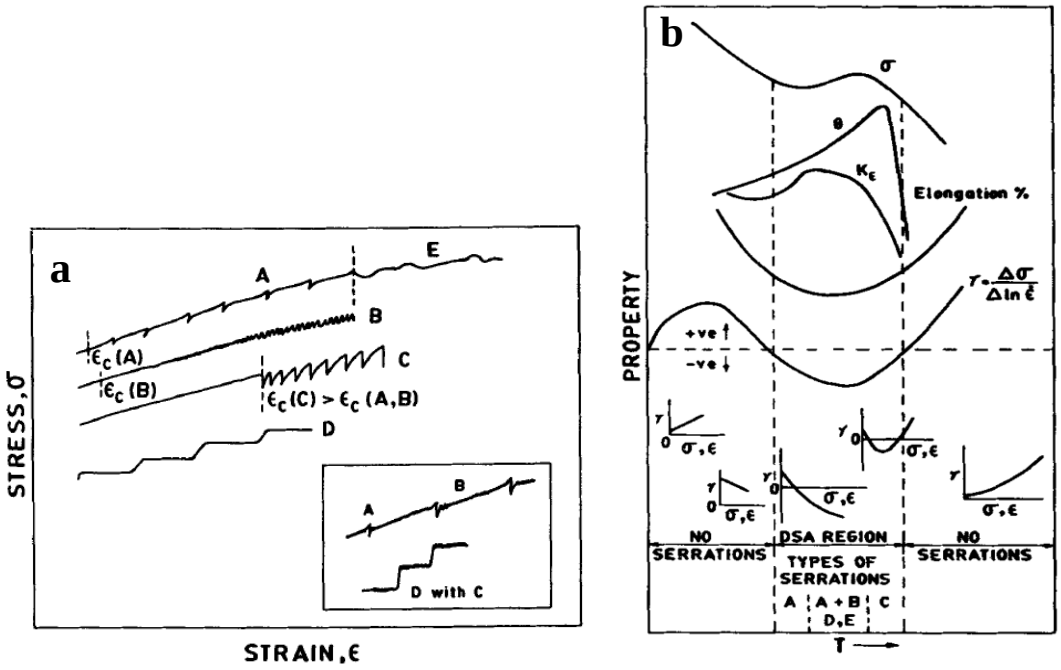

Fig. 1.12. (a) Types of serrations [46] (b) Schematic illustrations of various manifestations of DSA under monotonic loading [46,47].

Type C Serrations: These are yield drops that occur below the general level of the flow curve and are therefore considered to be due to dislocation unlocking. They occur at higher temperatures and lower strain rates than in the case of types A and B serrations.

Type D Serrations: These are plateaus in the stress strain curve due to band propagation similar to Luder–band with no work hardening or strain gradient ahead of the moving band front.

Type E Serrations: These are usually observed at high strains. These are similar to type A serrations, but with little or no work hardening during band propagation.

There are other manifestations of DSA, usually observed with respect to the specific temperature region under uniaxial loading, as summarized in the Fig. 1.12b showing peak/plateau in tensile and yield strength, minima in ductility, negative strain rate sensitivity etc. Figure 1.12b also shows the variation of strain rate sensitivity in the region of non DSA region.

As mentioned above, DSA considerably alters the mechanical properties of material, more importantly ductility is reduced which significantly affects other mechanical properties, particularly fatigue life. Thus, it is essential to assess the effect of DSA on fatigue life of the component. In the same manner as in uniaxial loading there are also characteristic features of DSA under cyclic loading, denoted by the variation of fatigue life, cyclic stress response and hysteresis loop behavior discussed below in the fatigue part. Usually an inverse dependence of peak tensile stress on strain rate and temperature; an unusual increase in cyclic hardening; and occurrence of serrated flow known as the Portevin–Le Chatelier (PLC) effect [48,49] are common features, suggesting DSA under cyclic loading.

1.7 Dynamic Strain Ageing in Cr–Mo Steels

1.7.1 Dynamic Strain Ageing in Cr–Mo Steels under Monotonic Loading

Different manifestations of DSA reported by several investigators include increased ultimate tensile strength, negative strain–rate sensitivity, reduced failure strain and serrations in the engineering stress–strain diagrams, higher dislocation density, increased work–hardening index (*n*) [50–52]

Effect of tempering temperature on DSA behavior of modified 9Cr–1Mo steel has been studied in the temperature range 25–450 °C, under strain rates of 2.3×10^{-5} to 2.3×10^{-3} s^{-1}. In one case normalizing treatment has been given at 1100 °C, tempering at 710 °C and in the other case normalizing at 1100 °C and tempering at 550 °C [53]. However, the increase in ultimate tensile strength and reduction in ductility were much higher in case of higher tempering temperature than that at the lower one. The work–hardenability in the higher temperature tempered condition was increased rapidly while that in the low temperature tempered condition remained unaffected. The smaller DSA effects in low temperature tempered condition than that tempered at higher temperature is attributed to fine precipitate particles in the former condition as compared to that in the later one, which act as more effective sinks and can cause much faster depletion of the solute atmosphere.

Tensile behavior of a modified 9Cr–1Mo (T91) martensitic steel has been investigated by loading/unloading tensile tests between 25 and 450 °C at strain rate of 4×10^{-4} s^{-1} and discussed in terms of activation volume, dislocation motion and DSA [54]. Depending on the temperature, the evolution of mechanical behavior is divided into three stages. *Stage 1: 290 K≤T≤420 K,* in this interval the normalized flow stress (σ/μ) and the normalized long–range back stress (X/μ) slightly decreased, on the other hand the activation volume for the two plateaus increased. The hardening parameters K

and n are slightly reduced and suggested a thermally activated deformation–mechanism as active mode of deformation. *Stage ii: 430 K≤T≤500 K,* σ/μ and X/μ increased slowly while the hardening parameters and the activation volume reached a maximal value. *Stage iii: 500 K≤T≤700 K,* is characterized by occurrence of DSA involving serrations on the tensile curves. The activation volume for the two plateaus was constant between these temperatures with values lower than those observed in the stage ii, suggesting that the thermally activated motion of the screw dislocations was then governed by DSA. Fig. 1.13 summarizes these three stages with the evolution of σ/μ and X/μ, activation volume (V) and *n* as a function of temperature.

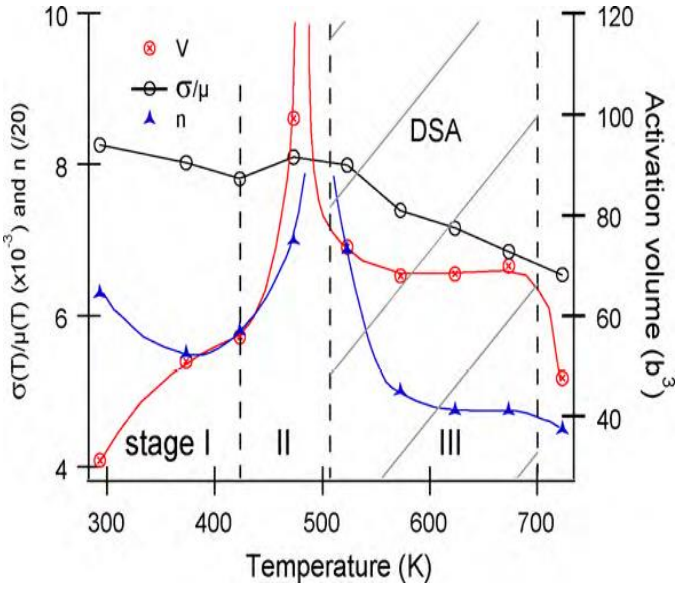

Fig. 1.13 The three stages of mechanical behavior with respect to temperature in modified 9Cr–1Mo steel [54].

1.7.2 Serrated Plastic Flow Behavior in Modified 9Cr–1Mo Steels

The effect of microstructure on the critical strain to onset of serrated flow at modified 9Cr–1Mo steel has been studied by Chandravathi et al [52] by soaking at different temperatures from 800–1350 °C and tensile testing at 300 °C. Soaking the

steel at different temperatures starting at a temperature below Ac_1 to temperature above Ac_4 followed by oil quenching and tempering at 760 °C for 1 h develops different microstructures in the steel with martensitic structure and different prior austenite grain sizes. The variation of prior austenite grain size and variation in inter barrier spacing with soaking temperatures is shown in Fig. 1.14 (a & b).

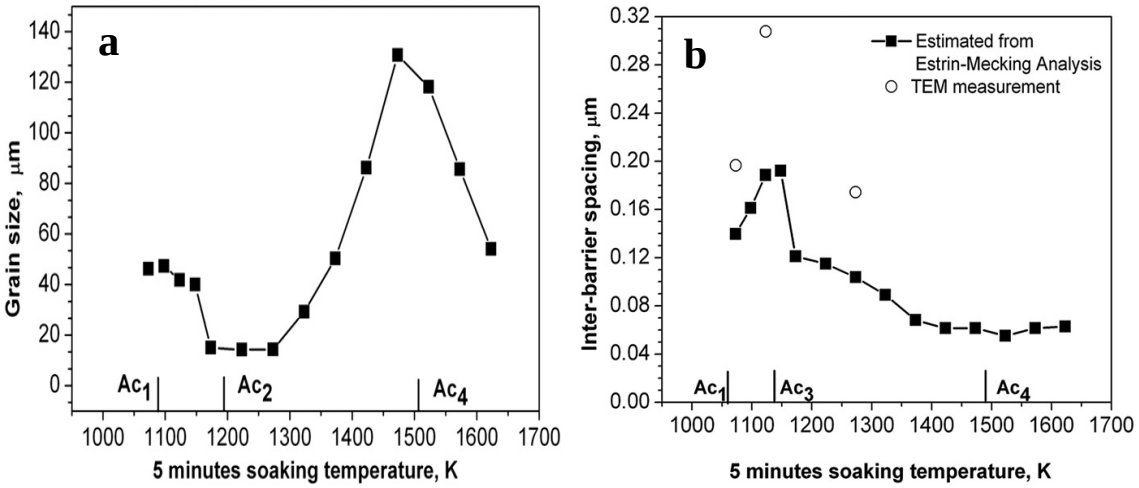

Fig. 1.14 (a) Variation of prior austenitic grain size after 5 min soaking at different temperatures (b) Variation of inter–barrier spacing of the steel following soaking at various temperatures [52].

Soaking the steel in the intercritical temperature range (between Ac_1 and Ac_3) showed lower hardness and tensile strength of the steel whereas soaking at temperatures above Ac_3 increased the hardness and tensile strength until the occurrence of relatively soft δ–ferrite for soaking at temperatures above Ac_4. Figure 1.15 shows load elongation plots with typical serration after soaking at different temperatures except for those having coarse prior austenite grains.

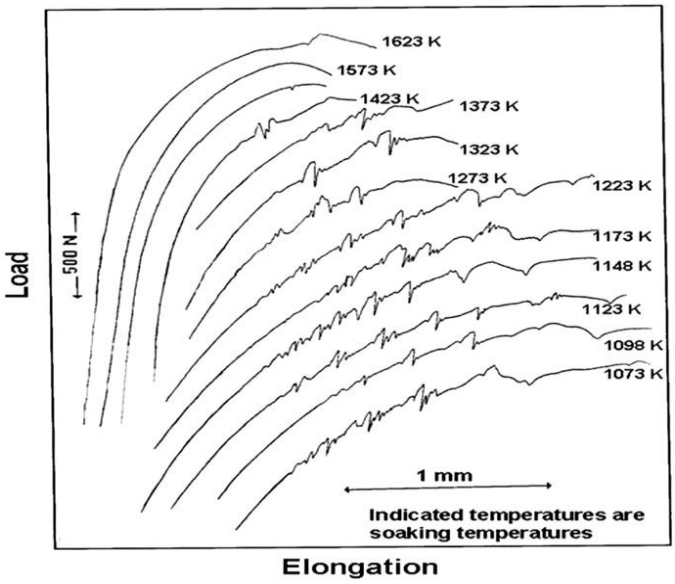

Fig. 1.15 Tensile curves of the steel soaked at different temperatures and tested at 300 °C [52].

The serrations were mostly of A and A+B type. The critical plastic strain to onset of serrated flow was found to increase with hardness of the steel which is influenced by different microstructures and has been attributed to decrease in inter–barrier distance to dislocation motion and also to increase in density of precipitate sinks for nitrogen.

Effect of silicon in modified 9Cr–1Mo steel (P91 grade) on DSA has been studied by conducting tensile tests between room temperature and 550 °C at a strain rate of 5×10^{-4} s^{-1} [50]. Amount of silicon was varied from 0.48 wt% to 1.88 wt%. A highest density of dislocation was obtained at 400 °C due to the formation of critical sized precipitates near grain boundaries, thus impairing the dislocation motion. Depending upon the silicon content the activation energy for serrated plastic flow was increased with increasing silicon content and varied from 64 and 80 kJ/mole.

The serrations in the stress–strain curves indicate specific interaction of the solute atmosphere with moving dislocations. This can be assessed by determination of

activation energy in the DSA regime. Usually a simple Arrhenius relationship between strain rate vs inverse temperature (semi logarithmic) plots in the DSA regime or based on measuring the critical strain for the onset of serrations were constructed to determine the activation energy. It is noticed that different activation energy values have been reported for the occurrence of DSA in 9Cr–1Mo steels, mainly due to change in composition and grain size of the steels [53], by measuring the height of the serrations, σ_d (stress decrement) against strain rate as suggested by [55] and activation energy of 45.1 $kJmol^{-1}$ (0.47 eV) was determined which is considerably less than those for lattice diffusion of nitrogen or carbon in alpha iron. Thus, in modified 9Cr–1Mo steels it is proposed that the initiation of serrations occurs by the formation of an interstitial nitrogen atmosphere on waiting dislocations by a pipe diffusion mechanism through forest dislocations. In another investigation by the same authors it is proposed that disappearance of serrated plastic flow in modified 9Cr–1Mo steels has been attributed to depletion of nitrogen content, at the dislocations below the critical concentration required to sustain the serrated flow due to diffusion of nitrogen from dislocation to the precipitate sinks [56].

The lower values of activation energy for DSA have been attributed to strain–induced diffusion [57] or pipe diffusion [58] along the dislocation core. Cuddy and Lesile [58] have suggested that substitutional solutes can diffuse rapidly along the dislocation core with the activation energy which may be 0.4–0.7 times the activation energy for bulk diffusion in α–Fe. The required features for the mechanism of DSA through pipe diffusion are provided by the dislocation arrest model [59], originally proposed by Sleeswyk [60]. This model suggests that solute atmospheres form on forest dislocations and, then, drain by pipe diffusion from forest dislocations to mobile dislocations while mobile dislocations are temporarily arrested at forest dislocations to

overcome them through thermal activation process (Fig. 1.16). Since this model does not require bulk diffusion through crystal lattice to form solute atmospheres on mobile dislocations, the lower activation energy, compared with that of bulk diffusion, can be understood. Pipe diffusion through the dislocation core will be rapid enough to allow formation of solute atmospheres on mobile dislocations without requiring any enhancement, since solute atmospheres need not pin the entire dislocation line to have an effect, but merely the portion of the dislocation line, intersecting with the forest dislocations.

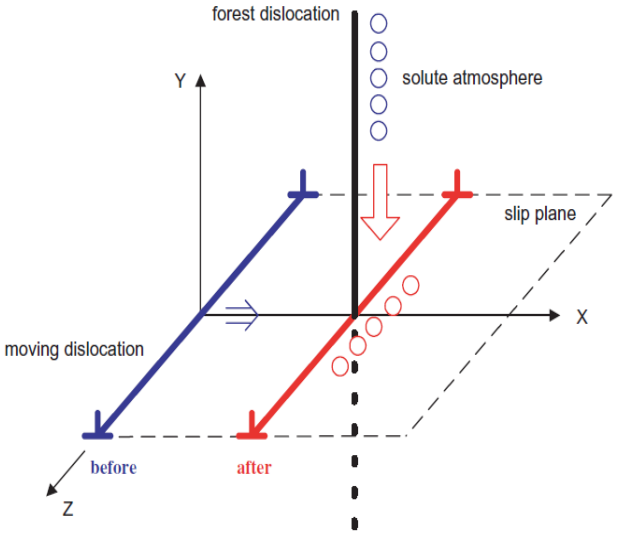

Fig. 1.16 Schematic, depicting the mechanism of DSA through pipe diffusion.

1.8 Microstructure Stability

High temperature strength of modified ferritic/martensitic steels mainly comes from the presence of fine precipitate particles of carbides and nitrides of Mo, Nb, Cr, and V inside and along boundaries of martensite laths and austenite prior austenite grain boundaries. For the long term application it is essential to have stable microstructure at

service temperatures. There have been various investigations on the ageing effect on the microstructural changes of advanced ferritic martensitic steels with 9–12%Cr. Figure 1.17 shows the growth and coarsening of precipitate particles in Grade 91 ferritic/martensitic steel. MX carbonitrides, containing Nb and V, remain essentially unchanged through creep service for long time (>100000h) at highest temperature of 650 °C. $M_{23}C_6$ carbides were found to be coarsening during creep service, while their average diameter remains below 250 nm at 600 °C. It was also observed that nucleation of Lave phase particles along the grain boundaries and their coarsening over a critical size, produces cavity formation and subsequently results in brittle intergranular fracture of the steel. The major cause of the reduction of long term creep resistance in 9%Cr Grades was mainly attributed to the high rate of coarsening of these Laves phases.

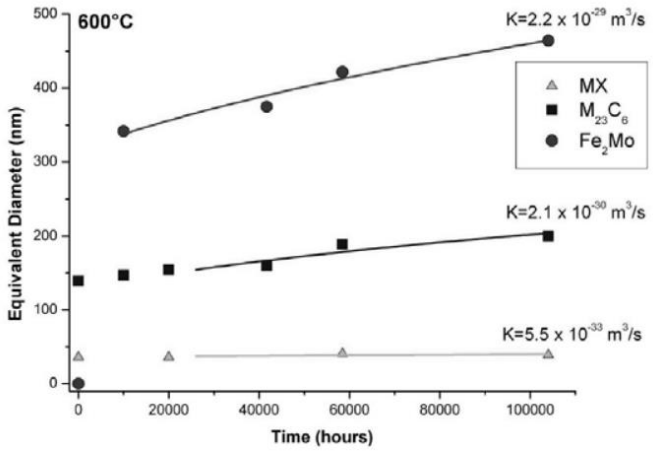

Fig. 1.17 Growth and coarsening of precipitate particles of Grade 91 ferritic/martensitic steel [61].

In 9%Cr steels very small amount of Z phase was recognized and no dramatic drop in volume fraction of MX was observed in association with the nucleation of the phase. Therefore, it is believed that the modified Z–phase does not affect negatively creep properties in the service temperature range of Grades 91, 92 and 92 of ferritic/martensitic steels [61].

1.9 Low Cycle Fatigue Behavior of Ferritic/Martensitic Steels

1.9.1 Cyclic Stress Response

Various aspects of low cycle fatigue behavior of modified 9Cr–1Mo steel in normalized and tempered condition such as effect of environment, grain size, ageing, processing, heat treatment, DSA have been studied by several investigators. However, most of the studies have been conducted at high temperatures of 500–650 °C at single strain rate and in the regime of high strain. Modeling of the cyclic stress response and fatigue life has also been reported by few investigators.

LCF of modified 9Cr–1Mo steel in normalized and tempered condition was studied at a strain rate of 10^{-3} s^{-1} at strain amplitudes from ±0.25% to ±0.60% at 550 & 600 °C by Kannan et al. [62]. Cyclic softening was reported and the rate of cyclic softening was found to be independent of strain amplitude.

Kim et al. [63] have also studied LCF behavior of this steel from RT to 600 °C. Cyclic softening was found not to change significantly in the temperature range of RT–500 °C but increased at 600 °C. The variation of microstructure and slip system, as a function of the number of cycles at total strain range of 1% at RT showed formation of dislocation cell structure after 100 cycles. The density of dislocations, cell size and lath width increased remarkably before 1000 cycles and did not change significantly after 1000 cycles. Cyclic softening was thus related to increase in lath width, the change from lath structure to dislocation cell structure, and the variation of slip system [63].

Total axial strain controlled continuous cycling tests were conducted between 500 and 600 °C at strain amplitudes of ±0.25%, ±0.4%, ±0.6% and ±1%. Softening was found to be strongly dependent on temperature, at elevated temperature [64]. Pronounced secondary hardening was observed by Vani et al.[65] at 600 °C for strain rate of 3×10^{-3} s^{-1} during the later part of fatigue life at strain amplitude of ±0.6%. In

another study it was revealed that precipitation of very fine secondary precipitates of probably V(C, N) occurred revealed during cycling that may be responsible for the secondary hardening [65]. The softening rate was independent of the external environment during testing and softening was attributed to annihilation of dislocations, rearrangement of laths into cells/subgrains and coarsening of carbides [66].

1.9.2 Cyclic Softening in Modified 9Cr–1Mo Steel Associated with Back Stress

It was reported in the literature that softening effect is mainly due to decrease of the back stress; the higher the strain amplitude, the stronger and faster was the softening effect at elevated temperatures. The isotropic stress is found to be independent of the strain amplitude, but increases when the temperature decreases. Whereas the viscous stress represents a large part of the total stress at 550 °C, it becomes almost negligible below 400 °C. Therefore, the decrease of the kinematic stress can be related to grain size effect. At 550 °C the mechanical softening effect is mainly due to a decrease of the back–stress at all the tested strain amplitudes. This behavior is compatible with TEM observations showing coarsening of the microstructure. The initial very fine martensitic microstructure becomes coarser and equiaxed, leading to a decrease in the Hall–Petch effect (due to dislocation pile–ups, subgrain size and subgrain misorientations [67]. The influence of the temperature was also studied, for T = 400 °C and below, the viscous stress is almost negligible, whereas the back–stress gets predominant as the temperature decreases. These changes in the cyclic stress repartition are compatible with the observation of stress localization (Intense Slip Bands) at room temperature (they were not yet observed at higher temperatures). Indeed as the number of activated slip systems increases to accommodate the plastic strain, the forest interactions get stronger [68].

Detailed investigation was carried out for understanding the physical mechanisms responsible for the cyclic softening. This mechanism was based on the

study of macroscopic hysteresis loops through the stress partition between isotropic, kinematic and viscous stress and detailed observations were made at the scale of conventional SEM (EBSD) and TEM at 550 °C. The softening effect is all the more pronounced and fast when the strain range is high at 550 °C. This softening behavior is due to disappearance of most of the microstructural subboundaries, characteristics of the tempered martensite and to decrease of the density of dislocations. This microstructural coarsening is heterogeneous for low applied strain and more homogeneous and pronounced when the applied plastic strain is high. The softening effect is directly correlated to the decrease of the kinematic stress. This type of stress arises from 'directional and long–range' obstacles to the movement of dislocations. Therefore, grain and subgrain boundaries (through a dislocation pile–up mechanism) and the microstructural heterogeneities (microstructure of dislocations, precipitates, etc.) are sources of kinematic hardening. This suggests that, during cycling, the softening effect comes from disappearance of microstructural heterogeneities [69].

1.9.3 Effect of Environment on Fatigue life

1.9.3.1 Liquid sodium

Liquid sodium has been chosen as the heat transfer medium in LMFBRs because of its high thermal conductivity and heat capacity. It remains liquid over a wide range of temperature. The use of liquid sodium requires assessment of the compatibility of structural materials with sodium.

Fatigue life was studied in air as well as in the flowing liquid sodium environment (Flow speed: 2.5 m/sec) at 600 °C [45]. The purity of sodium was controlled to very low levels of oxygen (less than 2 ppm). Influence of environment on fatigue life is shown in Fig. 1.18.

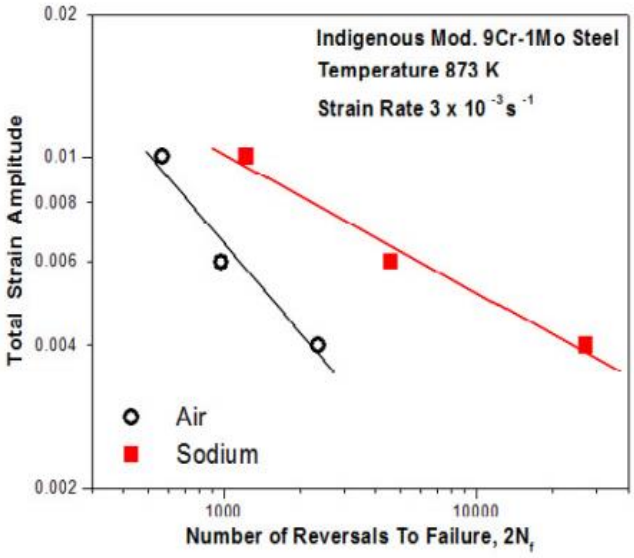

Fig. 1.18 Comparison of LCF life of modified 9Cr–1Mo steel in air and sodium environments at 550 °C [45].

It may be seen that fatigue life in liquid sodium is significantly higher and more pronounced at low strain amplitudes. The increase in fatigue life is considered to be due to absence of oxidation in high purity sodium environment which delayed the process of crack initiation and subsequent propagation stage [45]. Cyclic softening has been observed even in sodium environment as in air. Comparison of experimental lifetimes with RCC–MR design code predictions indicated that the design curve based on air tests is too conservative [70].

1.9.3.2 Vacuum

The effect of temperature of 500 °C & 550 °C was studied in vacuum under isothermal fatigue condition at strain amplitude of ±0.7% and strain rate of 10^{-4} s^{-1}. Fatigue life in vacuum was found to be independent of temperature. There was nearly a 2.5 times increase in fatigue life in vacuum in comparison to that in air suggesting the importance of the role played by oxides in reducing fatigue life [66]. An air

environment degrades low cycle fatigue properties with respect to vacuum at 538 °C [71].

1.9.3.3 Liquid Lead–Bismuth

Liquid metal embrittlement (LME) has been reported in a wide variety of solid metal/liquid metal couples, characterized by loss of ductility and fracture toughness of metallic materials when stressed in a specific liquid metal environment [72]. The low cycle fatigue behavior of modified 9Cr–1Mo ferritic–martensitic steel (T91) in stagnant liquid lead–bismuth eutectic (LBE) environment was studied at 160, 250, 350 and 400 °C for strain rate of 4×10^{-3} s^{-1} [73]. The variation of the fatigue lives with temperature shows a clear fatigue endurance "trough" in presence of LBE. The fatigue life decreased as the temperature was increased from 160 to 350 °C, however, a reverse behavior was observed from 350 to 450 °C. No such a strong temperature dependence of the fatigue limit was reported in vacuum for this steel. Also the fatigue life was found to be dependent on oxygen concentration in the LBE. A drastic reduction in fatigue life was observed with low oxygen concentrations LBE as compared to those in vacuum. Figure 1.19 shows effect of fatigue life in LBE and vacuum environment of modified 9Cr–1Mo steel (T91) at 350 °C. A mixed mode of fracture with intergranular and inter lath cracking was observed which was dependent on the orientation of the boundaries relative to the stress axis. The liquid metal embrittlement fracture has been characterized by three major features; quasi–brittle flat regions partially covered by nanodimples, numerous shallow secondary cracks propagating along the martensite lath boundaries and tear ridges covered by submicron dimples [74]. Quasi–cleavage fracture features were frequently observed on the fracture surfaces tested in the LBE environments. This is evidence of LME being able to intensely affect the fatigue crack propagation [75].

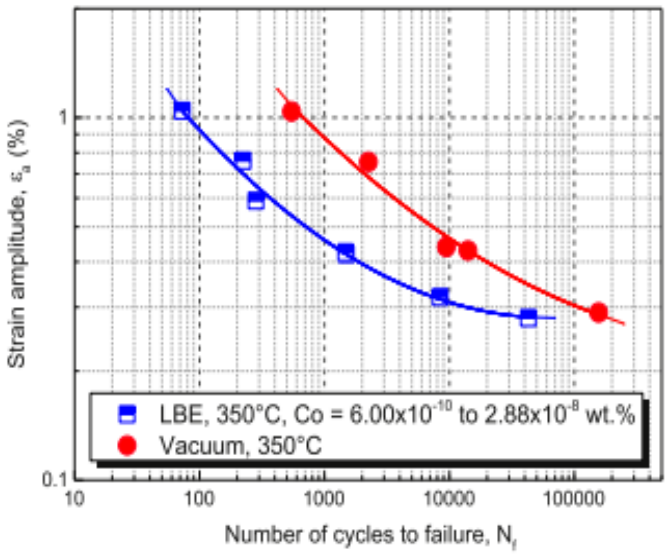

Fig. 1.19 Fatigue lives of T91 steel in an oxygen controlled LBE and in vacuum at 350 °C [74].

1.9.4 Effect of Thermal Ageing on LCF

The influence of thermal ageing on LCF life of forged modified 9Cr–1Mo steel was studied with and without notch at elevated temperature. There was no effect of the thermal ageing on low cycle fatigue life in the smooth specimen with each strain waveform. However, low cycle fatigue life of the notched specimen decreased by thermal ageing under load controlled condition with triangular and tensile compression–hold trapezoidal waveform [76].

Effect of pre-ageing between 482 and 704 °C for 5000 h of modified 9Cr–1Mo steel was studied at stain rate of 4×10^{-3} s^{-1} by Kim et al [77] in vacuum and compared with normalized and tempered condition. A series of specimens were aged for 5000 hours at one of several temperatures ranging between 482 and 704 °C, and then fatigued at the ageing temperature. Increase in ageing temperature decreased the stress amplitude. However, there was no effect of pre–ageing on fatigue life. Furthermore,

there was higher stress drop in pre–aged specimen in comparison to the normalized and tempered condition. There was no effect of temperature on fatigue life in vacuum [77].

On further increasing the ageing time to 50000 h and 75000 h at 538 and 593 °C, reduction in fatigue lives was observed. Ageing caused as–tempered carbide dissolution in material and/or reprecipitation together with additional precipitates of Laves (Fe_2Mo) phase, which removes some of the precipitate strengthening effects, and depletes solid–solution hardening effects on the dislocation network and subgrain boundary structure [40].

TEM analysis showed that stress free ageing at 593 °C resulted in disappearance of NbC carbides and reduction in volume fraction of VC carbides. These carbides are mainly responsible for the strength of the alloy in the N & T condition. Precipitation of Laves phase also occurs during ageing, removing Mo, which is potent solid solution strengthener and retardant to dislocation recovery/recrystallization [40]

1.9.5 Effect of Processing on LCF

Effect of processing routes forging and rolling on fatigue properties of modified 9Cr–1Mo steel had been studied at 538 °C. The hot forged materials with grain size of 31 μm exhibited inferior fatigue properties as compared to the fine grained hot rolled material with grain size of 19 μm, because in the large grain size material the fatigue initiation was adversely affected though it had little effect on the crack propagation stage [71].

1.9.6 Masing and Non–Masing Behavior in Modified 9Cr–1Mo Steels

Modified 9Cr–1Mo ferritic/martensitic steels in normalized and tempered condition have shown strong dependence of Masing and non–Masing behavior on strain amplitude. Krishna et al [78] studied this aspect at strain rate of 10^{-3} s^{-1} in the high strain

amplitude regime. At strain amplitude from ±0.7%to ±1.0% nearly Masing behavior was observed while at higher train amplitudes from ±1.1% & ±1.2% Non–Masing behavior was observed. Also at elevated temperature, stable hysteresis loop shows partial Masing behavior due to thermal activation [78]

1.9.7 Dynamic Strain Ageing in Modified 9Cr–Mo Steel under Cyclic Loading

As mentioned above DSA in monotonic loading, there are different DSA manifests during cyclic deformation including serrations in stress–strain hysteresis such as (i) large normalized cyclic hardening ($(\Delta\sigma/2)_{max}/(\Delta\sigma/2)_1$), where $\Delta\sigma/2)_1$ is the first cycle tensile stress amplitude and $(\Delta\sigma/2)_{max}$ is the maximum tensile stress amplitude, and the ratio increases with decreasing strain rate, (ii) An increase in the number of cycles to reach $(\Delta\sigma/2)_{max}$ with decreasing strain rate, (iii) For a given total strain range, plastic strain range decreases with increasing temperature or decreasing strain rate. (iv) increase in stress response with decreasing strain rate (negative strain rate sensitivity) or increasing temperature [47].

Influence of temperature (25 to 600 °C) and strain rate (3×10^{-2} s^{-1} to 3×10^{-5} s^{-1}) on LCF behavior of modified 9Cr–1Mo (hot rolled) ferritic martensitic steel in normalized and tempered condition, having average grain size of 30 μm, was studied at total strain amplitude of ±0.6%. The steels showed continuous cyclic softening at all the temperatures. LCF life at failure and at half–life is shown in Fig. 1.20. DSA was observed in the temperature range from 300 to 400 °C with indication of decreased fatigue life [79].

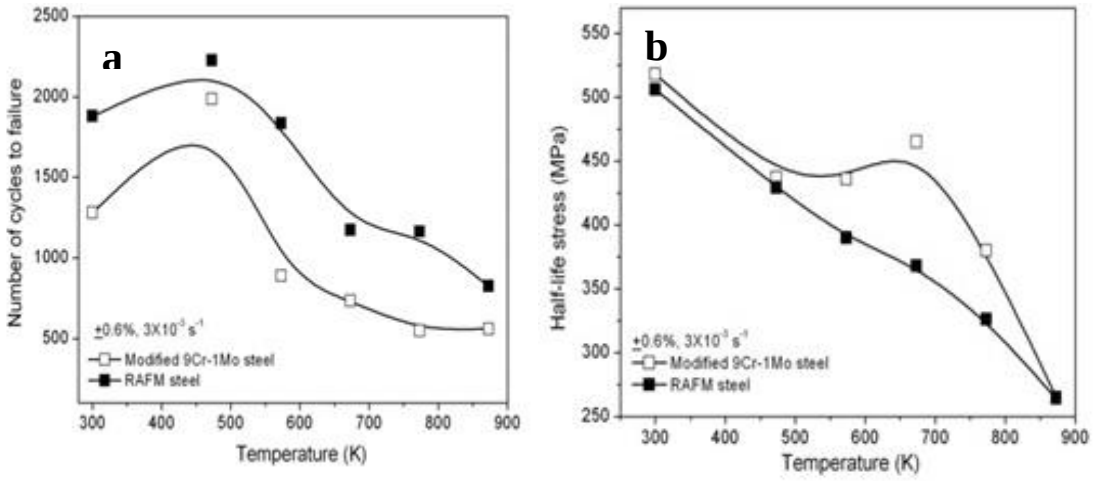

Fig. 1.20 Influence of temperature on (a) fatigue life and (b) half–life stress of modified 9Cr–1Mo and 1.4W–0.06Ta RAFM steels [79].

The influence of DSA pre–treatment on LCF behavior of modified 9Cr–1Mo steel was investigated at 550 °C. The DSA pre–treatment reduces the fatigue life, which is reflected on the fracture surface as multiple crack initiation and rapid crack propagation. The specimens pre-treated by DSA have higher peak tensile stress and positive mean stress effects, which is responsible for the lifetime reduction. The DSA pre-treatment does not change the cross–slip mode of cyclic deformation, however, results in accelerating the microstructure transformation from laths to cells and subgrains with low dislocation densities [80].

LCF behavior of hot rolled modified 9Cr–1Mo steel having prior austenite grain size was 50 µm was studied from RT to 600 °C, at strain rate of 3×10^{-3} s^{-1}, at different strain amplitudes varying from ±0.25% to ±1.0%. The alloy displayed certain evidences for the occurrence of DSA in the temperature range 500–600 °C. The alloy did not exhibit serrations in the plastic portions of stress–strain hysteresis loops in the temperature range examined [81]. However, serrations were noticed during LCF deformation at lower strain rate (3×10^{-4} s^{-1}) at 500 °C [82]. It has been pointed out that

the negative temperature dependence of plastic strain amplitude sets in much earlier than the appearance of serrated flow in fatigue under DSA conditions [83].

1.9.8 Creep Fatigue Interaction

Holding strain at peak position during the cyclic tensile and compression strain loading introduces combined effect of creep damage as well as LCF damage in the material, which significantly reduces the LCF life of the material. In service condition usually creep–fatigue interaction damage cycles take place during the steady state operation superimposed with LCF. Several evaluation methods are used based on ductility exhaustion concept for the prediction of creep–fatigue damage of this material under tension strain hold. A time–fraction type of linear damage summation concept based on a new ductility exhaustion theory is proposed from the point of view of its appropriate conservatism for time extrapolation and its simplicity. Also, a life reduction mechanism of low cycle fatigue with strain hold at the compression side is discussed, based on the data observed by scanning electron microscope [84].

Effect of hold time for 1 minute & 10 minute in tension and compression at peak strain for a total strain amplitude of ±0.6% had been studied at 600 °C in modified 9Cr–1Mo steel by Shankar et al. [65]. The fatigue life was found to decrease with increase in the duration of hold time in both tension and compression, with relatively higher damage during compression hold than that the tension hold. The reason for more damage during the compression hold than in tension hold has been attributed to detrimental effects of oxidation. Strain holding both in tension and compression in a fatigue cycle was found to be more damaging than tension or compression alone. The shorter life observed in tension plus compression hold conditions are comparable to those observed under longer duration hold in compression. The application of strain hold during cycling at elevated temperature accelerates the conversion of initial heavily

dislocated lath structure to equiaxed cells with low dislocation density and coarse carbides. [65].

In another investigation the effect of temperature was studied by Shankar et al. [64] at 550 and 600 °C holding both compression and tensile strain for a strain amplitude of ±0.6%. Compression strain holding exhibited lower fatigue life as compared to that in tension strain hold due to deleterious effect of oxidation. The more deleterious effect of oxides under compression hold was manifested as formation of more number of secondary cracks [64].

In case of creep fatigue interaction tests at 550 °C for a given fatigue strain range, at whatever the applied creep strain the softening effect falls along one single 'master curve'. This suggests that the microscopic phenomena responsible for the softening effect are directly related to the amount of plastic strain applied (glide of dislocations, climb and cross–slip). Finally the study of the macroscopic stress fall and the hysteresis loops revealed that the softening effect is directly related to the amount of cumulated (visco) plastic deformation experienced (for a given fatigue strain range) and to the level of heterogeneity of the microstructure. After pure fatigue at very low applied strain (±0.3%), some blocks of laths have recovered (very low density of dislocations and almost no subgrain visible) whereas most of the microstructure is unchanged. After creep–fatigue the microstructural recovery is much more homogeneous and all the more pronounced when the applied strain is high [69].

1.9.9 Finite Element Simulation Studies

There have been few investigations also on simulating the cyclic stress behavior of the modified 9Cr–1Mo steels using finite element modeling. Different hardening and softening models have been used to simulate the cyclic stress behavior. Low cycle fatigue behavior was studied at RT and 550 °C at strain rate of 10^{-3} s^{-1} for strain

amplitudes from ±0.3% to ±0.8%. Chaboche hardening model was employed considering elasto–plastic response of the material. The predicted hysteresis loops and cyclic stress response of the steel obtained from the FE analysis showed good agreement with experimentally obtained results [85].

A model for the cyclic stress behavior observed at elevated temperature (550 °C) in 9–12%Cr martensitic steels was proposed based on physical mechanisms described at the scale of slip systems. The microstructural recovery (decrease of the density of dislocations and subgrain coarsening) observed experimentally is explicitly formulated and introduced in a self–consistent homogenization scheme for the scale transition.

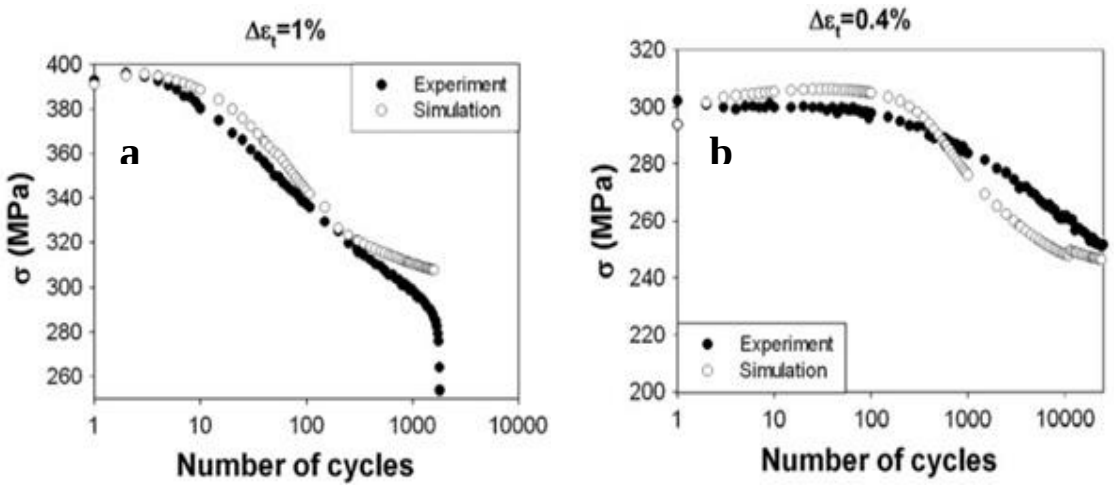

Fig. 1.21 Comparison between experimental and simulated cyclic softening: (a) $\Delta\varepsilon_t$ = 1% and (b) $\Delta\varepsilon_t$ = 0.4% [86].

The homogenization framework was selected in order to account for microstructural features like crystallographic orientation and neighborhood effects. Its relative complexity, added to a lack of experimental knowledge on the exact microstructural description of the material led to several drastic assumptions which were discussed and chosen in order to propose a first modeling approach. The

experimental and simulated cyclic stress response behavior of the steel at 1.0% and 0.4% strain ranges is shown in Fig. 1.21.The cyclic softening effect is very correctly predicted for total strain range of 0.4% in pure fatigue [86].

1.10 Scope of Investigation

Literature survey revealed that no correlation of DSA was established with deformation behavior of the modified 9Cr–1Mo steel. Also no detailed investigation has been carried out to understand the process of a typical rosette fracture occurring under tensile deformation in this steel. No investigations have been carried out on LCF behavior of this steel at lower temperatures particularly in the range of DSA. Little attention has been paid on LCF behavior at lower strain amplitudes. Only few studies are available on microstructure characterization of LCF tested specimens of the modified 9Cr–1Mo steel.

1.11 Objectives of the Present Study

- To establish the temperature range of dynamic strain ageing in the modified 9Cr–1Mo steel based on tensile properties, internal friction and deformation behavior.

- Detailed investigation related to occurrence of rosette fracture in tensile deformation and the role of different parameters like temperature, strain rate, microstructure and texture.

- Systematic investigation on LCF behavior of this steel at different temperatures; room temperature, 300 °C (DSA region) and 600 °C at strain rates of 10^{-2} s^{-1} & 10^{-3} s^{-1}.

- Detailed investigation on cyclic deformation behavior and fracture behavior of the material tested in LCF at different temperatures and strain rates.